Meshfree Simulations for Additive Manufacturing Process of Metals

Zongyue Fan & Bo Li

Integrating Materials and Manufacturing Innovation

ISSN 2193-9764

Integr Mater Manuf Innov
DOI 10.1007/s40192-019-00131-w

Springer

Your article is protected by copyright and all rights are held exclusively by The Minerals, Metals & Materials Society. This e-offprint is for personal use only and shall not be self-archived in electronic repositories. If you wish to self-archive your article, please use the accepted manuscript version for posting on your own website. You may further deposit the accepted manuscript version in any repository, provided it is only made publicly available 12 months after official publication or later and provided acknowledgement is given to the original source of publication and a link is inserted to the published article on Springer's website. The link must be accompanied by the following text: "The final publication is available at link.springer.com".

Author's personal copy

Integrating Materials and Manufacturing Innovation
https://doi.org/10.1007/s40192-019-00131-w

THEMATIC SECTION: ADDITIVE MANUFACTURING BENCHMARKS 2018

Meshfree Simulations for Additive Manufacturing Process of Metals

Zongyue Fan[1] · Bo Li[1]

Received: 19 January 2019 / Accepted: 18 March 2019
© The Minerals, Metals & Materials Society 2019

Abstract
We present a meshfree direct numerical simulation (DNS) capability for the additive manufacturing (AM) process of metals based on the hot optimal transportation meshfree (HOTM) method. The HOTM method is a meshfree thermomechanical Lagrangian computational framework for material behaviors under extreme thermomechanical loading conditions. It combines the optimal transportation meshfree (OTM) method and the variational thermomechanical constitutive updates. In the HOTM method, the linear momentum and energy conservation equations are solved simultaneously in a monolithic way. A phase-aware constitutive model is developed to predict the melting/solidification phase change of metals and multiphase mixing during the AM process automatically. The HOTM method is validated in the simulations of the laser welding process over Inconel 625 bare plate by applying heat flux models for the laser beam, the convective heat loss, and radiation heat loss. The performance measurements of the simulation results, including the melt pool geometric dimensions and cooling rates, are comparable to the experimental data measured in the AM benchmark tests. The influence of various laser powers and laser scanning speeds on the melt pool thermodynamics is also studied.

Keywords Meshfree · Additive manufacturing · AM benchmark test

Introduction

Additive manufacturing (AM) has drawn a lot of attention in recent years. In contrast to the traditional subtractive and formative manufacturing approaches, the optimal design for complex structures may be readily achieved with AM technologies. Nevertheless, there are still many challenges accompanied by this technology. Due to the high energy density deposited into the product in a short time, the melt pool thermal dynamics are transient and highly nonlinear. As the power beam scans over the surface of the solid material, it melts and vaporizes, which induces complex interactions between the solid/liquid/gas phases. Researchers have found that it is the processing parameters, such as the laser power, laser moving speed, and particle size, that determine the behavior of the melt pool, which further dominates the quality of additive manufactured products. A number of studies have been devoted to finding a relationship between processing parameters and product performance.

✉ Bo Li
bxl295@case.edu

[1] Department of Mechanical and Aerospace Engineering, Case Western Reserve University, Cleveland, OH 44106, USA

There have been many experimental studies concentrated on quality control conducted in recent years. Griffith et al. [1] study the influence of scanning strategies on additive manufactured Al-Si alloys and ways to obtain a good product quality. Thijs et al. [2] show that the laser scanning speed and hatch distance can influence the product quality for Ti6Al4V alloy and the microstructure evolution during this process. Wu et al. [3] study the effects of the laser scanning pattern, power, and speed on the residual stress for stainless steel. Dinda et al. [4] present the influence of different laser power and scanning speed on the material Inconel 625. Jia and Gu [5] study the effects of laser processing parameters on the microstructure and mechanical behavior for the superalloy Inconel 718. Most of these experiments rely on trial and error methods. They have found that there exists a "process window" for processing parameters, within which an acceptable product quality can be achieved. However, due to the nature of AM experiments, such as expensive machines, high-cost metal powder materials, and highly time-consuming, numerical simulations offer an efficient way to study the effects of AM processing parameters on the product quality rather than physical experiments.

The finite element method (FEM) and the volume of fluid (VOF) method are popular numerical methods for studying the AM processes (Yuan and Gu [6], Kubiak et al. [7]).

Published online: 11 April 2019

Author's personal copy

However, most of these simulations solve a heat transfer equation assuming the Fourier law and are limited by the grid resolution and difficulties in the Eulerian methods. The discrete nature of particles for the widely used powder bed fusion (PBF) based AM technology is usually not accounted for FEM simulations. The arbitrary Lagrangian-Eulerian (ALE) method (Khairallah et al. [8]) is applied to simulate the single track AM process at a mesoscopic scale. Nevertheless, the ALE simulations require frequent remeshing of the complex three-dimensional domain, dynamic tracking of the material interfaces, and remapping of the field data. The AM process is a strongly coupled thermomechanical fluid-structure interaction (TFSI) problem, which includes the phenomenon of phase transition and interaction between different material states. However, current mesh-based simulation capabilities are insufficient or unreliable to model the solid-liquid-gas phase transition and mixing process under high deformation and thermal rate, especially for the PBF process. In this paper, we present a pure Lagrangian meshfree solution for the high-fidelity prediction of the AM process, the hot optimal transportation meshfree (HOTM) method. The HOTM method is capable of taking into account most of the dominant underlying physics and solve the strongly coupled TFSI problem efficiently and robustly.

On the other hand, as discussed above, there are a number of experiments aiming to find the relationship between processing parameters and product quality. However, they are conducted over a variety of metals. And the ranges of the processing parameters (such as laser power and scanning speed) employed in these experiments are quite big. Thus, it is very difficult for numerical modelers to validate their simulation results. To solve this problem, the National Institute of Standards and Technology (NIST) held the AM benchmark test and provided a number of rigorous and highly controlled AM benchmark data to numerical simulation developers [9]. For simplicity, AM benchmark experiments were conducted on Inconel 625 bare plates. In this paper, the simulation results of the HOTM method are compared to the AM benchmark test data provided by NIST. The comparison is focused on the melt pool geometry and the cooling rate for an Inconel 625 bare plate under laser scanning.

Numerical Solver for Strongly Coupled TFSI Problems

The HOTM method combines the optimal transportation meshfree (OTM) method and a variational thermomechanical constitutive update for materials under extreme thermomechanical coupling conditions. It accounts for heat conduction, convection, and radiation within the finite deformation incremental Lagrangian framework. The pure Lagrangian nature of the HOTM method overcomes various challenges in the conventional models of AM processes. To describe the solutions of the AM process, the formulations of the HOTM method are introduced briefly in this section.

Governing Equations

The motion, deformation, and temperature distribution of a material system can be determined by solving the conservation laws, including the mass conservation:

$$(\rho \circ \varphi(X,t))J = \rho_0, \tag{1}$$

the linear momentum conservation:

$$\rho_0 \ddot{\varphi} = \nabla \cdot (P^e + P^v) + \rho_0 B, \tag{2}$$

the angular momentum conservation:

$$PF^T = FP^T, \tag{3}$$

and the energy conservation:

$$T\dot{N} = P^v : \dot{F} + Y \cdot \dot{Z} - \nabla \cdot q + \rho_0 Q \tag{4}$$

where ρ and ρ_0 is the current and reference density, respectively. $\varphi : \Omega_0 \times [t_0, t] \to \mathbb{R}^3$ is a time-dependent deformation mapping, $\boldsymbol{X}$ is the coordinate, $\boldsymbol{F}$ is the deformation gradient, $J = \det F$ is the Jacobian of the deformation, P^e is the equilibrium part of the first Piola Kirchhoff stress tensor and P^v is the viscous part, B is the body force per unit mass, T is temperature, N is the entropy per unit undeformed volume, $\boldsymbol{q}$ is the heat flux applied on the surface, Q is the distributed heat source per unit mass, and Y is the driving forces for the internal variables Z.

Variational Formulation

In order to develop the numerical solutions for the conservation laws, the weak form of the governing equations can be formulated by using the variational framework proposed in Yang et al. [10]. In the HOTM method, the variational structure is extended by taking into account the inertia term. This framework describes the corresponding action of a thermomechanical system with general dissipative mechanisms, which follows:

$$\begin{aligned} \Phi[\dot{\varphi}, T, \dot{Z}] = & \int_{\Omega_0} \left(\dot{K} + \dot{A} + N\dot{T}\right) dV \\ & + \int_{\Omega_0} \Delta\left(\frac{T}{\Theta}\dot{F}, \frac{T}{\Theta}\dot{Z}, -\frac{1}{T}\nabla_0 T; F, T, Z\right) dV \\ & - \int_{\Omega_0} \rho_0 B \cdot \dot{\varphi} dV - \int_{\Gamma_t} \overline{T} \cdot \dot{\varphi} dA \\ & + \int_{\Omega_0} \rho_0 Q \log\frac{T}{T_0} dV - \int_{\Gamma_q} q \cdot \hat{N} \log\frac{T}{T_0} dA \end{aligned} \tag{5}$$

where $K = \frac{1}{2}\rho_0 |\dot{\varphi}|^2$ is the kinetic energy, A is the Helmholtz free energy, Δ is the dissipation potential, $\hat{N}$ is the normal

Author's personal copy

direction. The state function $\Theta(F,T,Z)=\frac{\partial U}{\partial N}$ is derived from the internal energy, which can be treated as internal temperature, while T is the external temperature field. At the thermal equilibrium condition, the equation $\Theta = T$ is satisfied.

The Helmholtz free energy A includes the energy stored in the material due to heat capacity, W^h, which can be described as:

$$W^h = C(T)\left(T - T_0 - T\log\frac{T}{T_0}\right), \tag{6}$$

where $C(T)$ is the temperature-dependent specific heat. To take into account the effect of latent heat during phase change, the apparent heat capacity method is employed, such that $C(T)$ can be described as:

$$C(T) = C_{\text{phase1}}(1-\alpha(T)) + C_{\text{phase2}}\alpha(T) + \rho_0 L\frac{d\alpha}{dT}, \tag{7}$$

where $\alpha(T)$ is a phase transition function introduced to describe the smooth transition between two phases. L denotes the latent heat during the phase transition, C_{phase1} and C_{phase2} are the heat capacity coefficient of phases 1 and 2, respectively.

The dissipation potential Δ of Eq. (5) can be decomposed into three terms:

$$\Delta\left(\dot{F},\dot{Z},G;F,T,Z\right) = \phi^*\left(\dot{F};F,T,Z\right) + \psi^*\left(\dot{Z};F,T,Z\right) - \chi(G;F,T,Z) \tag{8}$$

where $G = -\frac{1}{T}\nabla_0 T$, ϕ^* is the internal dissipation potential, ψ^* is the viscous dissipation, and χ^* is the heat conduction dissipation potential.

This variational formulation works for materials with arbitrary constitutive relations including finite elastic and plastic deformation, rate-dependency, thermal softening, and strain hardening rules. Thus, the thermal and mechanical balance equations, the constitutive relations, and the equilibrium between the external temperature and the internal temperature can be obtained as the Euler-Lagrange equations by taking variations of the potential Φ and enforcing stationarity, i.e.,

$$\inf_{\varphi}\sup_{T}\inf_{Z}\Phi\left[\dot{\varphi},T,\dot{Z}\right]. \tag{9}$$

Optimal Transportation Meshfree Implementation

Li et al [11] propose the optimal transportation meshfree (OTM) method to discretize the variational framework for adiabatic systems. The OTM method is an incremental updated Lagrangian meshfree scheme capable of solving general fluid and solid flows, possibly involving multiple phases, viscosity, and general inelastic and rate-dependent constitutive relations, arbitrary variable domains with discontinuity and boundary conditions. The OTM method is constructed through integration of optimal transportation theory with local maximum entropy (LME) meshfree approximation and material point sampling [12].

The optimal transportation variational framework results in geometrically exact updates of the local volumes and mass densities, thus bypassing the need for solving a costly Poisson's equation for the pressure and eliminating the mass conservation errors that afflict Eulerian formulations. Furthermore, by adopting a discrete Hamilton principle based on a time-discrete action furnished by optimal transportation theory, the discrete trajectories have exact conservation properties including symplecticity, and linear and angular momentum. Material point sampling is introduced into the framework for spatial discretization. All the field information is carried by two sets of points, nodes, and material points, as shown in Fig. 1. In specific, the node $\boldsymbol{x}_{a,k}$ carries the kinematic information, such as displacement, velocity, and acceleration, while the local states of materials, such as strain, stress, material properties, and internal variables, are evaluated at the material point $\boldsymbol{x}_{p,k}$. The material point of the OTM method is very similar to the quadrature points in the FEM method, which provides an efficient way for numerical integration without a background mesh. The nodes and material points can be initialized by taking the nodes and barycenters of a conforming finite element mesh of the computational domain. The connection between material points and nodes is initialized by the connectivity table of the finite element mesh. Later in the calculations, the connection is dynamically reconstructed by using a search algorithm based on the deformation-dependent geometrical information.

We follow the same procedure as described in [11] for the discretization of the variational structure in Eq. (5). In particular, we consider the standard Ritz-Galerkin approach to approximate the displacement, temperature, deformation gradient, and thermodynamic force field using the local maximum entropy (LME) meshfree shape functions. The LME shape functions are affine on the boundary, which enables the direct coupling of solid/liquid/gas phases. In addition, the LME shape functions have the key property of possessing a Kronecker delta property at the boundary, which overcomes a common difficulty in meshfree approximation schemes and enables direct imposition of temperature boundary conditions on the domain without special treatment. To this end, the displacement and temperature field are interpolated by:

$$\varphi(X,t) = \sum\varphi_a(t)N_a(X) \tag{10}$$

$$T(X,t) = \sum T_a(t)N_a(X) \tag{11}$$

where φ_a is the nodal displacement, T_a is the nodal temperature, and N_a is the shape function of node $\boldsymbol{x}_a$.

Author's personal copy

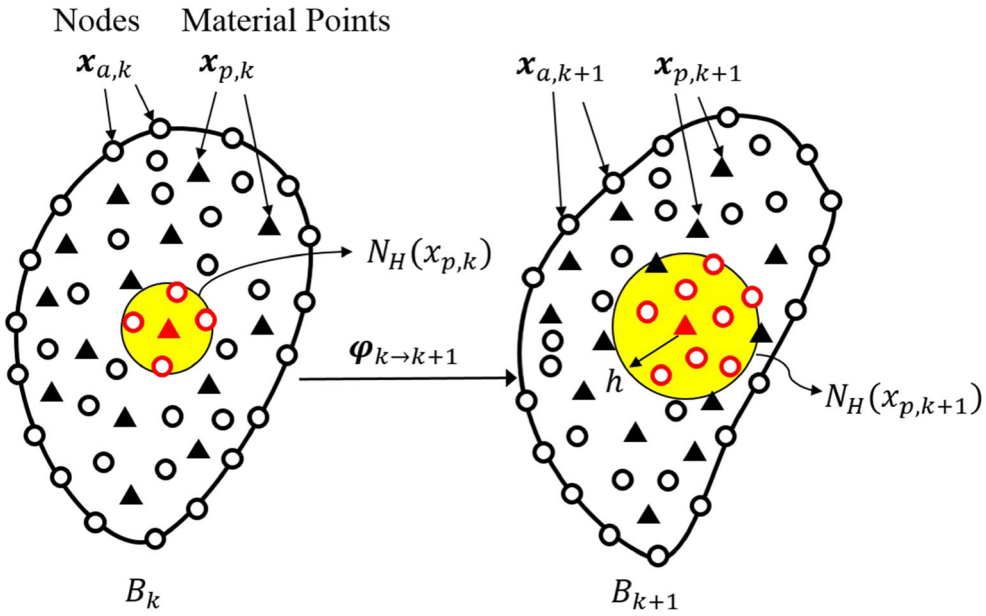

Fig. 1 Schematic of the OTM approximation scheme

Finally, variations of the semi-discrete incremental potential $\delta\Phi_n$ are taken. The stationarity conditions yield the fully discrete mechanical and thermal balance equations as:

$$f^{\text{int}}_{a,n+1} - f^{ext}_{a,n+1} = m_{a,n+1}\ddot{\varphi}_{a,n+1}, \tag{12}$$

$$Q^{\text{int}}_{a,n+1} - Q^{ext}_{a,n+1} = 0, \tag{13}$$

where $m_{a,n+1}$ denotes the lumped mass of the node $\boldsymbol{x}_a$ at t_{n+1}.

$$\ddot{\varphi}_{a,n+1} = \frac{2}{t_{n+1}-t_{n-1}}\left(\frac{x_{a,n+1}-x_{a.n}}{t_{n+1}-t_n} - \frac{x_{a,n}-x_{a,n-1}}{t_n-t_{n-1}}\right) \tag{14}$$

is a central difference approximation of the nodal acceleration.

The internal nodal force $f^{int}_{a,n+1}$ and external nodal force $f^{ext}_{a,n+1}$ can be obtained as:

$$f^{int}_{a,n+1} = \sum_p \left[\left(\frac{\partial A}{\partial F}(x_p) + \frac{\partial \phi^*}{\partial \dot{F}}(x_p)\right)\nabla N_a(x_p)\right] v_p, \tag{15}$$

$$f^{ext}_{a,n+1} = \sum_p \left[\rho_n B N_a(x_p)\right] v_p + \sum_{p\in\Gamma_t}\left[T(x_p)N_a(x_p)\right] A_p \tag{16}$$

where v_p is the volume of material point x_p.

The internal heat $Q^{\text{int}}_{a,n+1}$ and external heat $Q^{ext}_{a,n+1}$ are defined as:

$$Q^{int}_{a,n+1} = \sum_p -\left(\frac{\partial A}{\partial T}(x_p) + \frac{\partial \psi^*}{\partial T}(x_p)\Delta t\right) N_a(x_p) v_p - \sum_p \frac{\Delta t}{T_h(x_p)}\frac{\partial \chi}{\partial G_i}(x_p)\left(\frac{\partial N}{\partial x_i}(x_p) + G_i(x_p)N_a(x_p)\right) v_p \tag{17}$$

$$Q^{ext}_{a,n+1} = -\sum_p \left(\frac{\rho Q N_a(x_p)}{T_h}\Delta t\right) v_p + \sum_{p\in\Gamma_q}\left(\frac{H N_a(x_p)}{T_h}\Delta t\right) A_p \tag{18}$$

where $\boldsymbol{H}$ is the outward heat flux.

A fully explicit solution for Eqs. (12) and (13) faces stability issues, and the well-known Courant-Friedrichs-Lewy (CFL) conditions restrict the time step size [13]. Alternatively, a fully implicit method involves a very expensive calculation of the tangent of the mechanical forces, which is further exacerbated in large scale three-dimensional simulations. However, the time scale for heat transfer is much larger than the one required for the wave propagation in the material. In this paper, an operator splitting approach is used to construct a recursive staggering scheme for the solution of the strong thermomechanical coupling Eqs. (12) and (13). In specific, the mechanical balance equations are solved explicitly first based on the current temperature distribution. Assuming a constant motion, the thermal balance

Author's personal copy

equations are solved by an implicit method based on the Newton-Raphson solver to recompute the temperatures. The material properties are then updated according to the new resultant temperature field. The iterations increment until reaching the total simulation time.

Modeling the Additive Manufacturing Process

Boundary Conditions

To model the experiments conducted by the AM benchmark tests, i.e., the process of a laser scanning over an Inconel 625 bare plate, various heat flux models are introduced as the boundary conditions. First of all, the laser beam is modeled as a heat flux applied to the surface of the domain. The most widely used heat flux model in the field of AM is a Gaussian distributed heat flux with scanning velocity [14], which is given by:

$$q = \frac{2AP}{\pi r^2}\exp\left(-2\frac{(x-x_c(t))^2 + (y-y_c(t))^2}{r^2}\right) \tag{19}$$

where A is the absorptivity of the heat flux by the AM material, P and r are the power and radius of the laser beam, respectively, and $x_c(t)$ and $y_c(t)$ is the current location of the center of the laser spot. The profile of the Gaussian heat flux is shown in Fig. 2. $x_c(t)$ and $y_c(t)$ in Eq. (19) can be described by any time-dependent functions. Therefore, it furnishes an effective means of controlling the movement and scanning strategies of the laser beam in the simulations, such as the stripe hatch, the meander hatch, and the island scan strategy. The influence of various scanning speed on the deformation of the melt pool is studied in this paper by adopting different $x_c(t)$ and $y_c(t)$ in the heat flux model. In addition, the shape, power, and other important processing parameters of the power beam can also be easily manipulated to study their relations to the melt pool dimensions.

The energy loss due to convective heat transfer between the plate and the atmosphere is not negligible. In our simulations, a convective heat flux is applied on the plate. As observed in experiments, this flux can cool down the melt pool. The convective heat flux takes the simple form as:

$$q = C(T(x_a) - T_0) \tag{20}$$

where C is the convective coefficient and T_0 is the temperature of the environment.

Radiation heat flux is another boundary condition applied on the surface nodes of the domain. The Stefan Boltzmann law,

$$R = \sigma\varepsilon\left(T(x_a)^4 - T_0^4\right), \tag{21}$$

is employed. Here, the Stephan's constant $\sigma = 5.669 \times 10^{-8} W/m^2K^4$ is employed. The emissivity ε varies with temperature and surface chemistry in physical experiments. For simplicity, the average value of the emissivity is adopted for the solid state and the liquid state of the material, respectively.

A Phase-Aware Constitutive Model

To predict the stress at material points, a phase-aware thermomechanical constitutive model is developed, since the AM process involves multiphase transitions and interactions. The temperature T directly determines the local state of the material point. That being said, a material point is in solid phase with a local temperature lower than the melting temperature. As the temperature increases beyond the melting or boiling temperature, it automatically transfers to the liquid phase or gas phase, which is accomplished by using temperature-dependent material coefficients in the multiphase constitutive relations. For instance, the material model of the

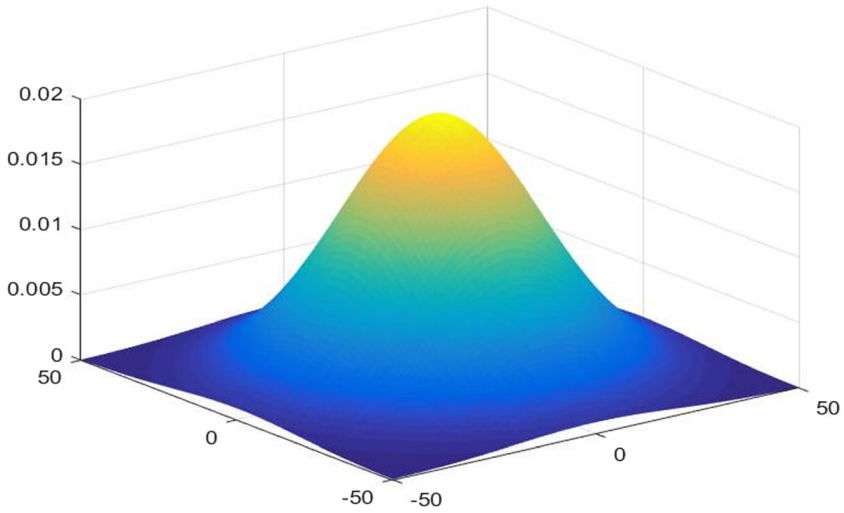

Fig. 2 The profile of Gaussian distribution

Author's personal copy

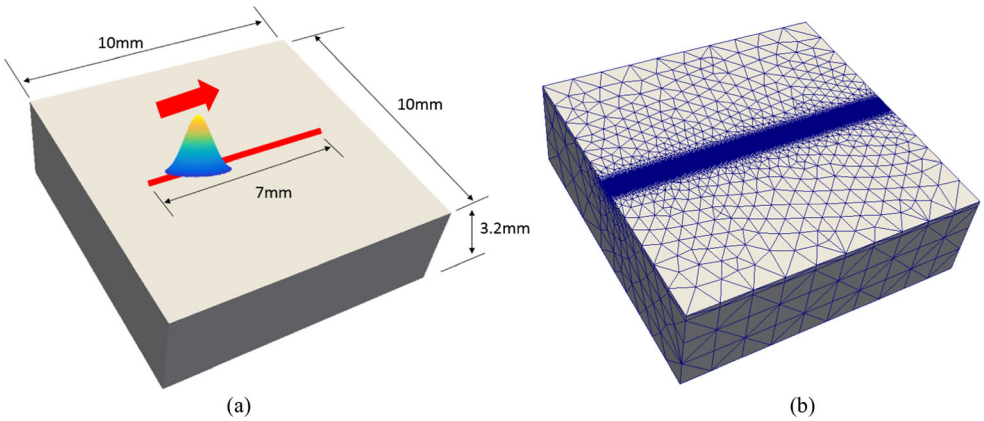

Fig. 3 The geometry and mesh of the specimen

solid state is assumed of the thermoelastic form:

$$\sigma_{ij} = \frac{K(T)}{2}\left(J - (1 + 3\alpha\Delta T)\frac{1}{J}\right)\delta_{ij} + 2\mu(T)\varepsilon_{ij}^{dev}, \tag{22}$$

where $K(T)$ is the temperature-dependent bulk modulus, J is the Jacobian, α is the linear thermal expansion rate, ΔT is the temperature difference between the material point temperature T_p and the reference temperature, δ_{ij} is the Kronecker delta, $\mu(T)$ is the temperature-dependent shear modulus, and ε_{ij}^{dev} is the deviatoric strain. As the material point transfers to the liquid state, the viscoelastic model with Murnaghan-Tait equation of state is employed [15], i.e.,

$$\sigma_{ij} = \left(-\frac{C}{\gamma}(J^{-\gamma} - 1) - P_0\right)\delta_{ij} + 2\eta(T)\dot{\varepsilon}_{ij}, \tag{23}$$

where C is a constant related the bulk modulus of the liquid, which is usually taken between 7×10^6 and 7×10^7 Pa to allow for compressibility, γ is a material parameter and equals to 7 for water, P_0 is the ambient pressure, $\eta(T)$ is the temperature-dependent viscosity, and $\dot{\varepsilon}_{ij}$ is the strain rate. The last term in Eq. (23) corresponds to the viscous stress. For liquid phase, shear modulus automatically goes to zero.

Simulation Results and Discussion In this paper, the comparison of simulation results and the experimental data is focused on the melt pool geometric dimensions and the cooling rate. For simplicity, external forces, such as gravity or recoil pressure, are not considered in the simulations. The deformation of the melt pool is mainly due to the thermal expansion of the material.

Table 1 Processing parameters for three lasers

Case	Radius (μm)	Power (W)	Scan speed (m/s)
A	85	137.9	0.4
B	85	179.2	0.8
C	85	179.2	1.2

Model Setup

The model geometry is shown in Fig. 3a. The dimensions of the domain are 10 mm × 10 mm × 3.2 mm. The geometry is modeled by an adaptive mesh with mesh size ranged from 25 to 1000 μm, as shown in Fig. 3b, which leads to 244,624 elements. Since the HOTM method is a meshfree method, the mesh is only used to determine the location of the material points and nodes as described in the "Optimal Transportation Meshfree Implementation" section. After the initialization, the connectivity between material points and nodes will be updated automatically throughout the simulations.

The AM benchmark tests are conducted using two different machines, and the laser parameters used by each machine are different. Our simulation results are compared against

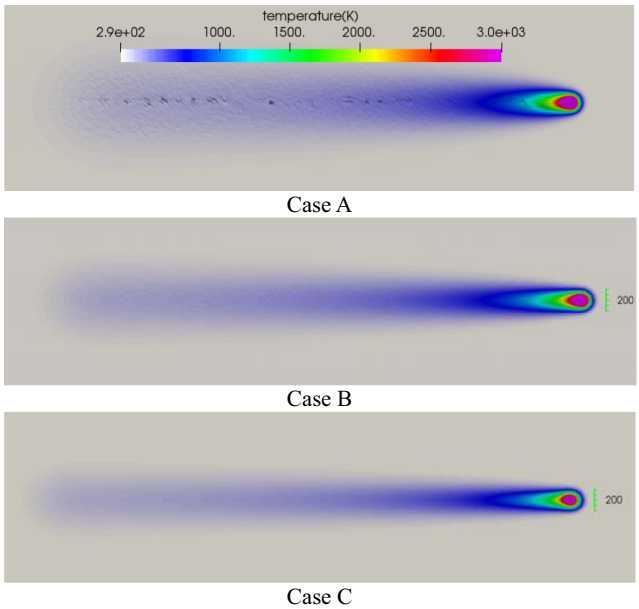

Fig. 4 Final predicted temperature distributions for cases A to C

Author's personal copy

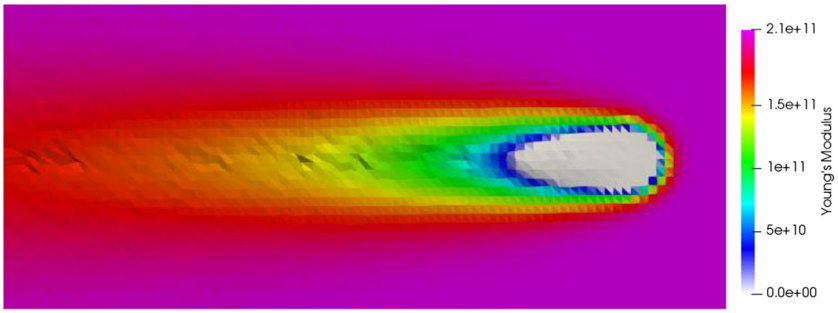

Fig. 5 Young's modulus of the melt pool and surrounding area

experimental data measured from the AMMT machine. Three AM benchmark experiments are simulated using the HOTM method. For each case, a laser with different laser power and scanning speed is adopted. The parameters of these three types of lasers are shown in Table 1. Only one single laser scan track is simulated in each case. Particularly, the scan track at the center of the plate is 700-μm long and performs from left to right, as shown in Fig. 3a.

Due to the lack of material property data for Inconel 625 in liquid and gas state, constant heat conductivity and heat capacity are employed for all the material states of Inconel 625. The heat conductivity is set as 20 W/m K, and the heat capacity 600 J/kg K. The laser absorptivity of the material is set to be 20%, as listed in [14]. The emissivity of the material is set as 0.8, as the measure in experiments.

Simulation Results

The final predicted temperature distribution for the three different laser scan tracks is shown in Fig. 4. From this figure, it can be found that even though the laser has moved away for a relatively long time, the temperature remaining on the scan track is still high. The scan track of case A is the widest. We can also see that the laser scan track becomes thinner as the laser scanning speed increases, which is consistent with the melt pool width data as shown in the following sections. The deformation of the melt track can be observed in Fig. 4, where the melt track expands due to the effect of thermal expansion. The volumetric deformation of case A is the biggest among these three cases, and the one of case C is small. This is due to the low scanning speed of the laser in case A. Even though the laser of case A has the smallest laser power, the energy deposited into the geometry for case A is the highest among all the tests.

The temperature-dependent Young's modulus for the material in the area near the melt pool is shown in Fig. 5. The area where Young's modulus becomes zero represents the melt pool. Thus, the melt pool will deform more easily than other regions of the domain. The temperature-dependent Young's modulus also contributes to the expansion of the melt track.

The transverse cross-sections of the melt pool in each case are shown in Fig. 6. From the temperature plot, we can see that the depth of the melt pool decreases from case A to case C. And the expansion of the melt pool is also decreasing from case A to case C, as the surface of the melt pool of case A is much higher than the surrounding. However, for case C, the deformation of the melt pool is negligible. It is evident that the thermodynamic behavior of the melt pool is strongly sensitive to the laser scanning speed.

The melt pool geometry as defined by the solidus temperature 1563 K (1290 °C) in the AM benchmark test is shown in Fig. 7. As illustrated from our simulation results, the melt pool

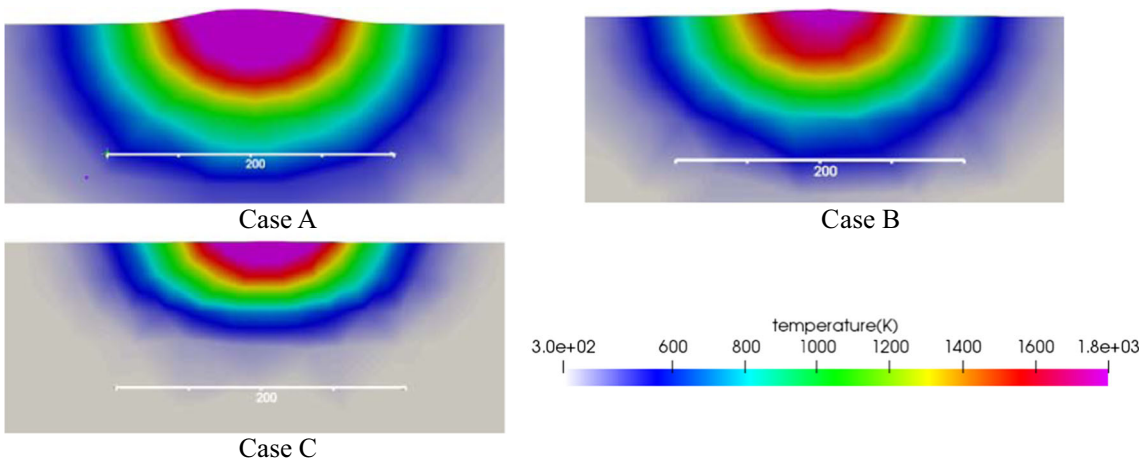

Fig. 6 The transverse cross-section of the melt pool

Author's personal copy

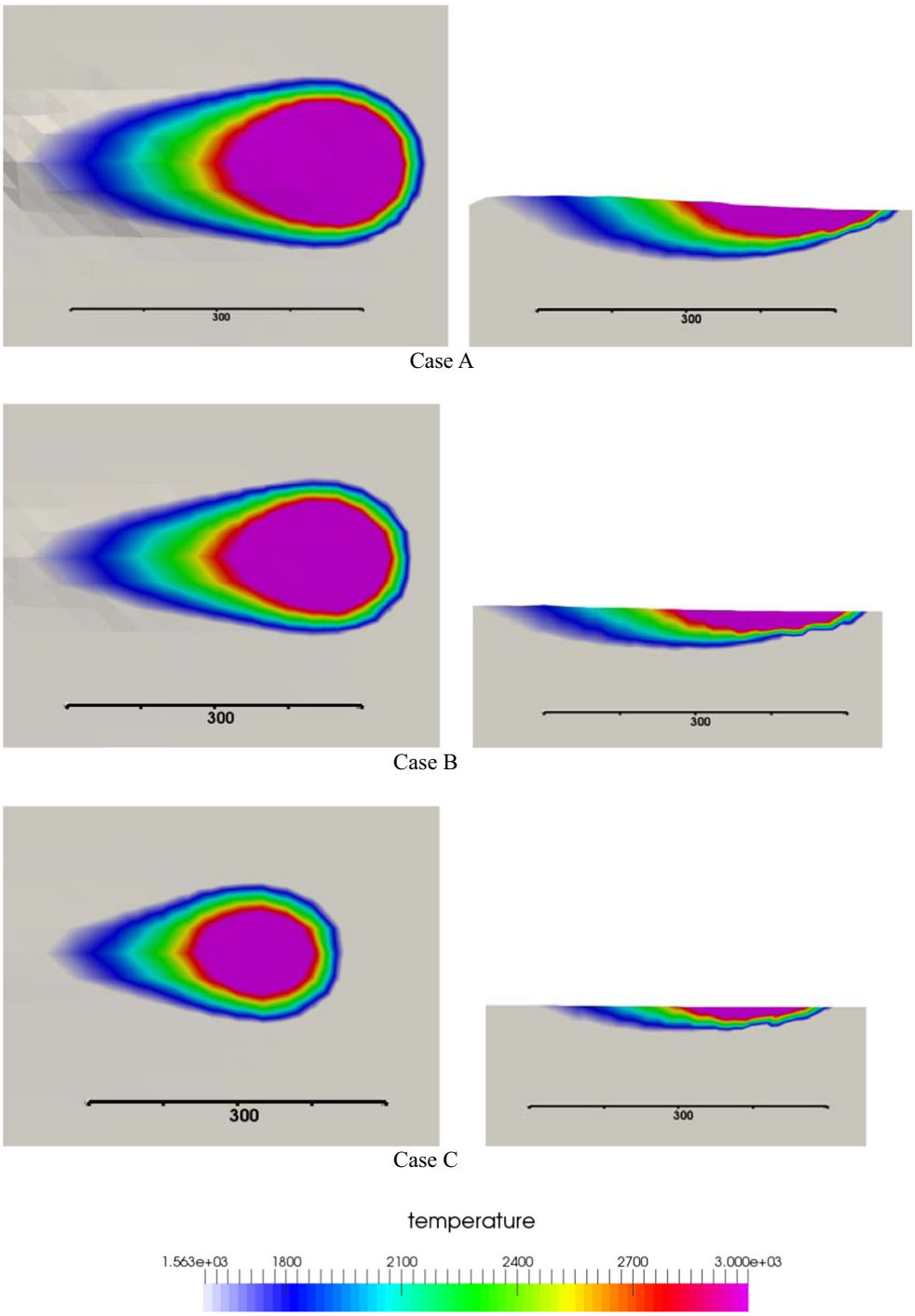

Fig. 7 The predicted geometry of the melt pool for each laser case. The left pictures are the top view, and the right pictures are the cross-sections of the melt pool along the laser scan direction

Table 2 The dimensions of the melt pool for each case, as defined by the solidus temperature

	Calculated length (μm)	Measured length (μm)	Calculated width (μm)	Measured width (μm)	Calculated depth (μm)	Measured depth (μm)
Case A, 137.9 W, 0.4m/s	339.57	300	167.7	147.9	47.48	42
Case B, 179.2 W, 0.8m/s	346.7	359	150	123.5	36.13	36
Case C, 179.2 W, 1.2m/s	275.9	370	137.43	106	24	29.6

Author's personal copy

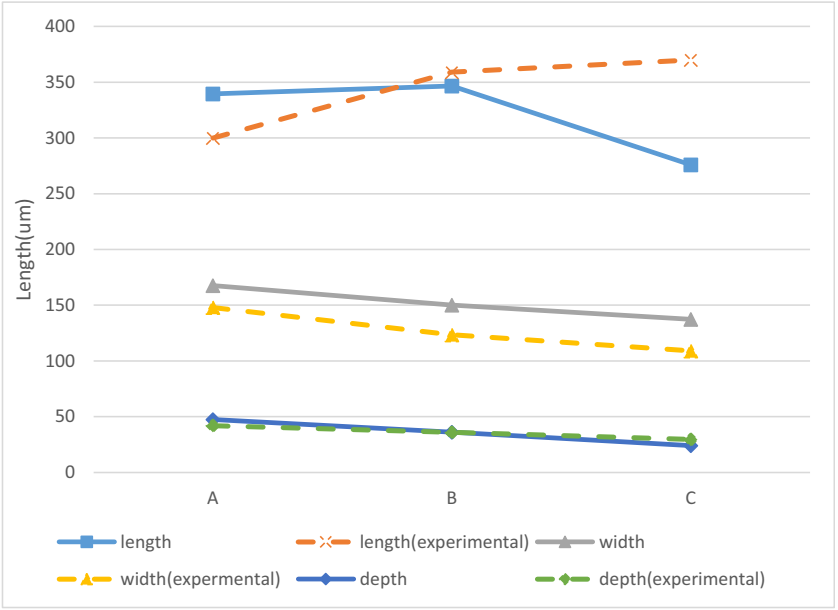

Fig. 8 Comparison of simulation results of the melt pool geometry (length, width, and depth) with experimental data

geometry becomes steady after the first 200 μm laser scanning. It can be observed that the length of melt pool increase from case A to case B and decreases from case B to case C. The comparison between the geometric dimensions predicted in our simulations and measured from experiments is summarized in Table 2. The data is also plotted in Fig. 8. Solid lines represent the simulation results and dash lines for experimental data. It is worth mentioning that the predictions are comparable with the experimental measurements. Figure 7 demonstrates that the width of the melt pool decreases from case A to case C. This result is consistent with the data measured from experiments as shown in Table 2. The laser scanning speed dominates the melt pool width for these three cases. As the scanning speed increases, the energy deposited into the material decreases. So there is less energy concentrated in the area surrounding the laser center, which leads to the decreasing of the melt pool width.

From Fig. 7, we can also find that the expansion of the melt pool appears at the area near the trailing edge of the melt pool. This is because the material at the leading edge of the melt pool cannot deform instantly when the laser flux first scans over it. After the laser moves away and the leading edge becomes trailing edge, the melt pool starts the expansion slowly. Thus, the surface from the leading edge to the trailing edge of the melt pool is a slope, as shown in Fig. 7.

In the experiments, the melt pool length keeps increasing from case A to case C, while the calculated value reaches the maximum in case B. However, the laser scanning speed increases from case B to case C when the power remains the same, so the energy deposited into the material may decrease. As a consequence, the length of the melt pool might decrease. The inconsistency may be because of missing physics in our simulation framework, such as the vaporization and recoil pressure.

To predict the cooling rate, the temperature distribution along the center line of each scanned track after the trailing edge of the melt pool is obtained. In AM benchmark experiments, the cooling rate is calculated only for the range 1000~1290 °C (1273~1563 K). The equation for calculating the cooling rate used by the AM benchmark test is:

$$\text{cooling rate} = \frac{dT}{dt} = \frac{1563-1273}{(d_1-d_2)/v} \tag{24}$$

where d is the corresponding coordinates for the indicated temperature, and v is the laser scanning speed. The predicted cooling rate and measured values in experiments for each case are summarized in Table 3. It is evident that the cooling rate increases from case A to case C. Thus, for these three cases, the faster the laser scans, the higher the cooling rate of the scan track will be.

Table 3 The predicted cooling rate for each laser case

Case	Predicted cooling rate (K/s)	Measured cooling rate (K/s)	Standard deviation (experimental) (K/s)
Case A 137.9 W, 400 mm/s	1.37×10^6	1.16×10^6	2.68×10^5
Case B 179.2 W, 800 mm/s	2.29×10^6	1.08×10^6	5.88×10^5
Case C 179.2 W, 1200 mm/s	3.48×10^6	1.90×10^6	5.52×10^5

Author's personal copy

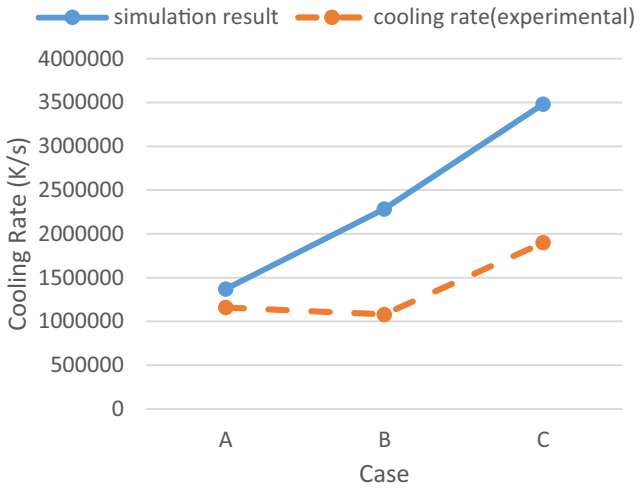

Fig. 9 The cooling rate for case A, case B, and case C

The data of Table 3 is also plotted in Fig. 9. We can see that the simulated cooling rate of case A is very close to the corresponding experimental cooling rate. However, the discrepancy between the simulated cooling rate and experimental data in case B and case C is notable. The inaccuracy of the thermal properties might be the reason for the discrepancy. More calibrations are needed for the thermal conductivity, heat capacity, and convective heat transfer coefficient. Table 3 also lists the standard deviation of cooling rates measured from experiments. The large deviation implies significant uncertainties of the experimental data for cases B and C. This might be another cause of the inconsistency between the simulation results and experimental data. It is noteworthy in Fig. 9 that the trend of the predicted cooling rates is consistent with the one in physical experiments as the laser parameters varying from case A to case C.

Conclusion and Future Work

A pure Lagrangian numerical solver for strongly coupled thermomechanical problems, the hot optimal transportation meshfree (HOTM) method, is developed to simulate the complex physics of the additive manufacturing process. The simulation results of the HOTM method are compared with the experimental data provided by the AM benchmark test at NIST. It can be concluded that the simulation results of HOTM are comparable with experimental data. The maximum error in the predicted length is 25%. The discrepancy between experimental data and simulation results may be caused by a number of reasons. More calibrations of the temperature-dependent material properties are needed to improve the accuracy of the simulation results. The surface tension effects will be included in the variational framework as traction boundary conditions to take into account the Marangani effect. In the future, the HOTM method will be applied in the powder-scale modeling of powder bed fusion based AM processes, rather than simulations of the laser scanning process on a bare metal plate.

Funding Information This project is financially supported by the National Science Foundation (NSF/CMMI Career Award 1652839).

References

1. Griffith ML, Keicher DM, Atwood CL, Romero JA, Smugeresky JE, Harwell LD, Greene DL (1996) Free form fabrication of metallic components using laser engineered net shaping (LENS). In: Solid Freeform Fabrication Proceedings, vol. 9, pp. 125–131
2. Thijs L, Verhaeghe F, Craeghs T, Van Humbeeck J, Kruth JP (2010) A study of the microstructural evolution during selective laser melting of Ti–6Al–4V. Acta Mater 58(9):3303–3312
3. Wu AS, Brown DW, Kumar M, Gallegos GF, King WE (2014) An experimental investigation into additive manufacturing-induced residual stresses in 316L stainless steel. Metall Mater Trans A 45(13): 6260–6270
4. Dinda GP, Dasgupta AK, Mazumder J (2009) Laser aided direct metal deposition of Inconel 625 superalloy: microstructural evolution and thermal stability. Mater Sci Eng A 509(1–2):98–104
5. Jia Q, Gu D (2014) Selective laser melting additive manufacturing of Inconel 718 superalloy parts: densification, microstructure and properties. J Alloys Compd 585:713–721
6. Yuan P, Gu D (2015) Molten pool behaviour and its physical mechanism during selective laser melting of TiC/AlSi10Mg nanocomposites: simulation and experiments. J Phys D Appl Phys 48(3): 035303
7. Kubiak M, Piekarska W, Stano S (2015) Modelling of laser beam heat source based on experimental research of Yb:YAG laser power distribution. Int J Heat Mass Transf 83:679–689
8. Khairallah SA, Anderson AT, Rubenchik A, King WE (2016) Laser powder-bed fusion additive manufacturing: physics of complex melt flow and formation mechanisms of pores, spatter, and denudation zones. Acta Mater 108:36–45
9. Lane B, Heigel J, Zhirnov I, Khromschenko V, Ricker R, Phan T, Stoudt M, Mekhontsev S, Levine L (2019) Measurements of melt pool geometry and cooling rates of individual laser traces on IN625 bare plates. Integr Mater Manuf Innov
10. Yang Q, Stainier L, Ortiz M (2006) A variational formulation of the coupled thermo-mechanical boundary-value problem for general dissipative solids. J Mech Phys Solids 54(2):401–424
11. Li B, Habbal F, Ortiz M (2010) Optimal transportation meshfree approximation schemes for fluid and plastic flows. Int J Numer Methods Eng 83(12):1541–1579
12. Arroyo M, Ortiz M (2006) Local maximum-entropy approximation schemes: a seamless bridge between finite elements and meshfree methods. Int J Numer Methods Eng 65(13):2167–2202
13. Courant R, Friedrichs K, Lewy H (1967) On the partial difference equations of mathematical physics. IBM J Res Dev 11:215–234
14. King WE, Anderson AT, Ferencz RM, Hodge NE, Kamath C, Khairallah SA, Rubenchik AM (2015) Laser powder bed fusion additive manufacturing of metals; physics, computational, and materials challenges. Appl Phys Rev 2(4):041304
15. Ganzenmüller GC, Steinhauser MO (2011) The implementation of smooth particle hydrodynamics in LAMMPS. Paul Van Liedekerke, and Katholieke Universiteit Leuven

Publisher's note Springer Nature remains neutral with regard to jurisdictional claims in published maps and institutional affiliations.